Journal of Power Sources 196 (2011) 5651–5658

Contents lists available at ScienceDirect

Journal of Power Sources

journal homepage: www.elsevier.com/locate/jpowsour

Self-assembled mesoporous $LiFePO_4$ with hierarchical spindle-like architectures for high-performance lithium-ion batteries

Yang Xia, Wenkui Zhang*, Hui Huang, Yongping Gan, Jian Tian, Xinyong Tao*

College of Chemical Engineering and Materials Science, Zhejiang University of Technology, Hangzhou 310014, China

ARTICLE INFO

Article history:
Received 15 October 2010
Received in revised form 4 January 2011
Accepted 17 February 2011
Available online 4 March 2011

Keywords:
Lithium iron phosphate
Hydrothermal synthesis
Mesoporous
Hierarchical architecture
Nanocrystal
Li ion battery

ABSTRACT

Self-assembled mesoporous $LiFePO_4$ (LFP) with hierarchical spindle-like architectures has been successfully synthesized via the hydrothermal method. Time dependent X-ray diffraction, scanning electron microscopy, and cross section high resolution transmission electron microscopy are used to investigate the detailed growth mechanism of these unique architectures. Reaction time and pH value play multifold roles in controlling the microstructures of LFP. The LFP particles are uniform mesoporous spindles, which are comprised of numerous single-crystal LFP nanocrystals. As the cathode material for lithium batteries, LFP exhibits high initial discharge capacity (163 mAh g^{-1}, 0.1 C), excellent high-rate discharge capability (111 mAh g^{-1}, 5 C), and cycling stability. These enhanced electrochemical properties can be attributed to this unique microstructure, which will remain structural stability for long-term cycling. Furthermore, nanosizing of LFP nanocrystals can increase the electrochemical reaction surface, enhance the electronic conductivity, and promote lithium ion diffusion.

1. Introduction

Since olivine-type lithium iron phosphate $LiFePO_4$ (LFP) was first reported as positive electrode materials for rechargeable lithium batteries by Padhi et al. [1], it has received widespread attention as a promising cathode material owing to its low cost and environmentally benign nature of Fe as well as the excellent chemical stability and safety imparted by the covalently bonded PO_4 groups. However, LFP is an insulating material, the main disadvantages of LFP material are the poor electronic conductivity [2–4] and slow lithium-ion diffusion [5,6], which are addressed as two major issues to be solved before it could be used in large-scale commercial applications. To overcome the demerits, tremendous efforts have been made to enhance the electronic and ionic conductivity of LFP particles through various material processing approaches, such as carbon coating [7–9], metal-ion doping [10–13], and reducing particle size [14–16]. In particular, it has been proved that carbon-coated LFP particles with nano size and homogeneous distribution could effective shorten the diffusion length for electrons and lithium ions and increase reaction areas to make the full utilization of LFP for charge and discharge [17–20].

Up to now, various methods have been developed to prepare homogenous carbon-coated LFP nanoparticles, such as sol–gel method [21,22], co-precipitation [23,24], mechanochemical activation [25,26], spray technology [19,27] and hydrothermal/solvothermal synthesis [28–33]. Among these methods, hydrothermal method offers many advantages of mild synthesis conditions, high degree of crystallinity, high purity and narrow particle size distribution of product. So it is a very popular method to synthesize nanoscale LFP building blocks including nanoparticles, nanorods, and nanoplates [28,29,31–34]. Furthermore, many recent efforts have been focused on the hierarchical assembly of novel LFP architectures from nanoscale building blocks, which is a crucial step toward the realization of functional nanosystems and offers opportunities to study its electrochemical properties. However, there are only few reports related to the microscale hierarchical architecture of LFP particles. Yang et al. [35] found that a hierarchical dumbbell-like architecture of LFP showed an excellent cycling stability. Qian et al. [36] synthesized nanoembossed mesoporous LFP microspheres which exhibited remarkable electrochemical performance. Uchiyama and Imai [37] believed that fagot-like and sheaf-like LFP mesocrystals could be suitable for the application to high-rate performance. Rangappa and co-workers [38] reported that flower-like LFP hierarchical microstructures could be favorable for obtaining high capacity and good cyclic performance. Recently, Teng et al. [39] reported that hierarchical LFP nanodendrites with good cycling stability demonstrated its potential application for lithium-ion batteries. Nevertheless, the aforementioned works often use expensive organic solvents and surfactants, and need complicated processes. Therefore, it is still a great challenge to explore effective routes for the self-assembly of

* Corresponding authors. Tel.: +86 571 88320394; fax: +86 571 88320394.
E-mail addresses: msechem@zjut.edu.cn (W. Zhang), tao@zjut.edu.cn (X. Tao).

0378-7753/$ – see front matter © 2011 Elsevier B.V. All rights reserved.
doi:10.1016/j.jpowsour.2011.02.044

novel hierarchical LFP architectures with excellent electrochemical properties.

In this work, we report a new kind of hierarchical architecture of LFP synthesized via a facile hydrothermal method, which has an interesting mesoporous spindle-like structure. The roles of reaction time and pH value in hydrothermal route were evaluated, and the mechanism of LFP particle growth was elucidated. Benefiting from this unique microstructure, the spindle-like LFP displays excellent lithium storage properties.

2. Experimental

2.1. Materials and preparation

LFP samples with spindle-like microstructures were prepared by a hydrothermal method. In a typical procedure, 12 mmol of $LiOH{\cdot}H_2O$ and 4 mmol of $FeSO_4{\cdot}7H_2O$ were first separately dissolved into 20 mL of 0.2 mol L^{-1} H_3PO_4 solution and 20 mL of 0.1 mol L^{-1} L-ascorbic acid solution. Subsequently, the $LiOH/H_3PO_4$ solution was added into the $FeSO_4$/L-ascorbic acid solution. After magnetic stirring at room temperature for 5 min, pH value of the precursor suspension was controlled by adding ammonia solution. Then the resulting suspension was placed into a 50 mL Teflon-lined stainless steel autoclave and maintained at 180 °C for 20 h. After the autoclave cooled to room temperature, the products were separated centrifugally, washed with de-ionized water and absolute ethanol, dried in oven at 80 °C for 12 h. To remove the adsorbed water, the LFP sample was heated at 650 °C for 4 h under flowing H_2/N_2 atmosphere (200 mL min^{-1}, 10 vol.% H_2 and 90 vol.% N_2).

2.2. Characterization

The phase purity and crystalline structure of the samples were characterized by a X-ray diffraction (XRD) using X'Pert Pro diffractometer with a step size of 0.02° for Cu Kα radiation (λ = 1.5418 Å). The particle size and morphology were observed by scanning electron microscope (SEM, Hitachi S-4800), transmission electron microscope (TEM, FEI Tecnai G2 F30) and high resolution TEM (HRTEM). The cross section HRTEM specimens were prepared by slicing LFP particles embedded in epoxy resin with a Reichert-Jung Ultracut E Ultramicrotome.

2.3. Electrochemical measurement

Electrochemical performances of LFP samples were investigated using a CR2025 coin-type cell assembled in an argon-filled glove box. To prepare the cathode, active material (LFP), acetylene black and polyvinylidene fluoride (PVDF) binder were mixed according to the ratio of 70:20:10 by weight. The mixture was dispersed in *N*-methylpyrrolidone and the resultant viscous slurry was cast on aluminum foil and dried at 120 °C under vacuum for 12 h. After that, the cells were assembled with lithium foil as the anode, LFP as cathode and 1 M $LiPF_6$ solution in a mixture of ethylene carbonate (EC) and dimethyl carbonate (DMC) with a volumetric ratio of 1:1 as the electrolyte.

Electrochemical capacity measurements were conducted on a Neware Battery Test System with galvanostatic charge and discharge in the voltage range of 2.5–4.2 V at room temperature. Cyclic voltammograms (CV) and electrochemical impedance spectroscopy (EIS) tests were performed with a CHI 650b electrochemical work station. CV tests were examined in the voltage range of 2.5–4.2 V at a scan rate of 0.1 mV s^{-1}, and EIS tests were carried out with the frequency ranging from 0.1 Hz to 100 kHz.

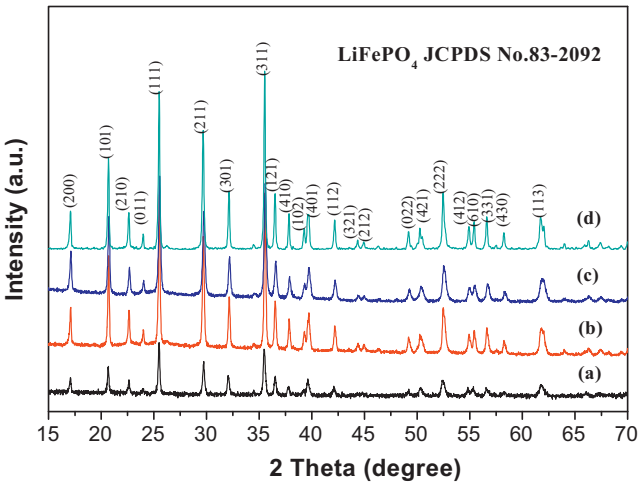

Fig. 1. XRD patterns of LFP with different pH values (a) pH 7; (b) pH 8; (c) pH 9; (d) pH 10.

3. Results and discussion

3.1. Structural and morphology characterization

Fig. 1 shows XRD patterns of the LFP obtained from the precursor at different pH values. All the samples are single phase of LFP, which can be indexed to the orthorhombic olivine type structure (JCPDS No. 83–2092). No impurities such as Li_3PO_4, which often can be found in the LFP product prepared by traditional routes [40], can be detected. Moreover, the intensity of the peaks increases along with the increase of the pH value of the precursor. High pH conditions are favorable to the precipitation of Li_3PO_4 and the hydrolysis of $FeSO_4$, which could stimulate the crystallization of LFP. Similar results have been reported by Wang et al. [41].

Fig. 2 shows SEM images of the synthesized LFP under different pH conditions. The morphologies of the final LFP samples are found to be sensitive to the pH values. The sample obtained at neutral pH condition is composed of large amounts of dispersed, flat and rhombus shaped nanocrystals as shown in Fig. 2a. When the pH value is increased to 8, an interesting morphological change of LFP can be observed. The sample is mainly composed of spindle like particles with *ca.* 2 μm in length and 1 μm in width (Fig. 2b). In addition, abundant primary nanocrystals can also be found in Fig. 2b. In the case of pH = 9, the particles exhibit similar morphology as that of pH = 8 (Fig. 2c). However, the ends of particles appear to be broad, and some ends are open as indicated by the arrows in Fig. 2c. Finally, spindle-like hierarchical architectures of LFP are obtained under pH = 10, and few primary nanocrystals can be observed (Fig. 2d).

In order to investigate the internal microstructure of spindle-like LFP particle, cross section TEM was conducted. Fig. 3 shows the schematic illustration of the cutting direction and the corresponding SEM and TEM images of spindle-like LFP. As shown in Fig. 3b and c, the spindle-like LFP is self assembled from many nanocrystals, which are *ca.* 100 nm in length and 50 nm in width. It is worth mentioning that these hierarchical architectures cannot be destroyed into fragments or dispersed nanocrystals even after 10 min ultrasonic treatment. This may be attributed to the L-ascorbic acid, which remains on the surface of the primary nanocrystals, will transform into amorphous carbon after high-temperature heat treatment. And these carbons will play a role of connecting the primary nanocrystals. Thus the spindle-like LFP particles possess excellent structural stability, which is very important for the cycling stability of commercial batteries. In addition, the internal microstructure of spindle-like LFP particle can be clearly

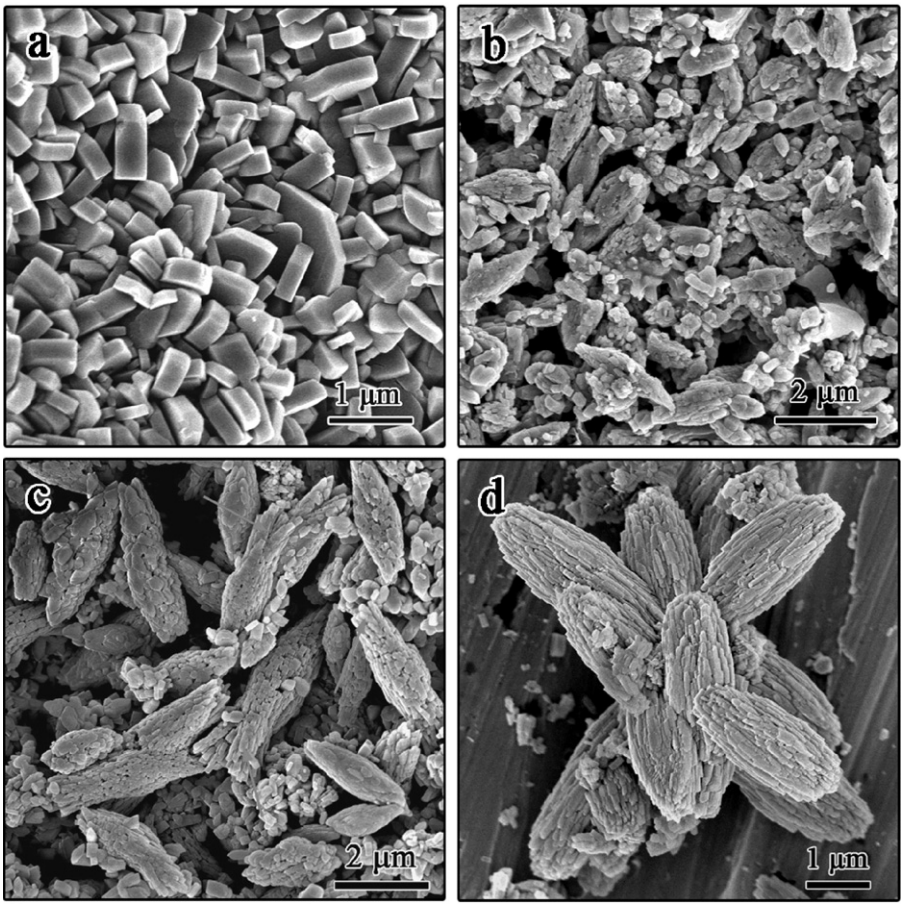

Fig. 2. SEM images of the obtained LFP samples with different pH values (a) pH 7; (b) pH 8; (c) pH 9; (d) pH 10.

seen from Fig. 3b and c that the nanocrystals are attached to each other and form an interesting mesoporous structure. It is well known that the porous structure could allow the electrolyte to penetrate into the positive materials and make the full utilization of LFP for charge and discharge [8,36,42].

The growth orientations and the grain boundaries of the nanocrystals in the hierarchical architectures were further studied. Fig. 4a shows a typical TEM image of spindle-like LFP particles. Fig. 4b is a higher magnification TEM image of the end of spindle-like LFP. It can be seen that the spindle-like LFP is hierarchically assembled with nanocrystals, which nestle together in a close-packed array. Fig. 4d is an HRTEM image taken from the particle in Fig. 4b. The measured fringe spacing values are 0.3476 and 0.3082 nm, corresponding to (1 1 1) and (−2 −1 1) planes of orthorhombic phase LFP. In addition, the inset in Fig. 4d shows the corresponding Fast-Fourier-Transform (FFT) pattern of the HRTEM image, which displays a single-crystalline pattern with sharp diffraction spots. And this result also proves that the

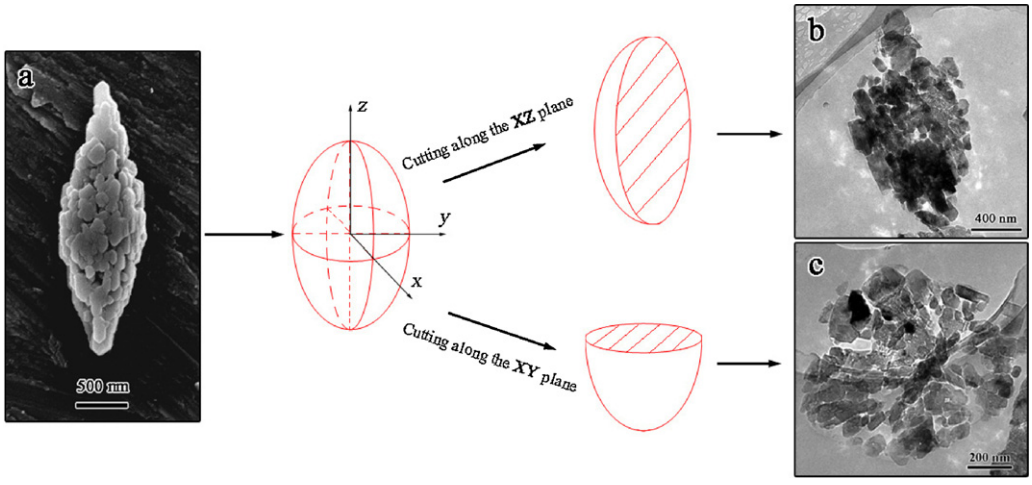

Fig. 3. Schematic illustration of the cutting direction. (a) SEM image of spindle-like LFP sample. (b and c) The cross section TEM images of spindle-like LFP sample along two different cutting directions.

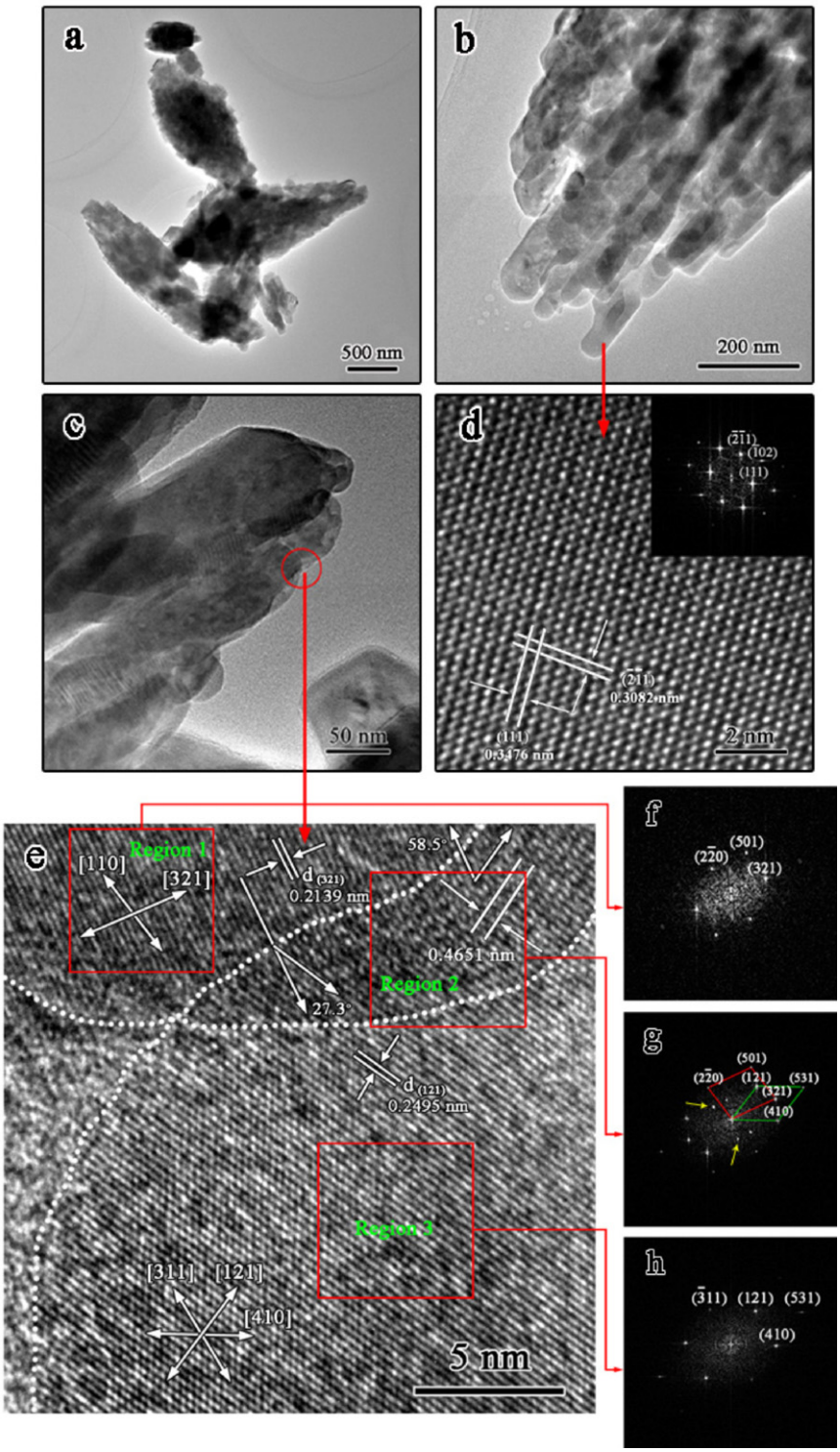

Fig. 4. TEM images of the spindle-like LFP particles. (a) A low-magnification TEM image of the spindle-like LFP particles. (b and c) A part of an individual particle. (d) HRTEM image of the spindle-like LFP particles in (b), the inset is the corresponding fast Fourier transform (FFT) image. (e) HRTEM image of the interface of two LFP grains. (f–h) The corresponding FFT images of region 1–3 in (e).

primary nanocrystals are well crystallized with pure olivine LFP phase.

Fig. 4c is a cross section TEM image of several compactly arranged nanocrystals. As marked in a red circular area, an interesting grain boundary (GB) can be observed. Fig. 4e is the corresponding HRTEM image of the GB. As can be seen from the image, there are three different regions which are indicated by the dotted curves. To further clarify the microstructure and the internal relationships of these regions, the corresponding FFT images are carried out (Fig. 4f–g). The ordered lattice fringes in the region 1 and 3 (Fig. 4e) and their corresponding FFT patterns (Fig. 4f and h) reveal that the grains in region 1 and 3 are single crystals. Fig. 4g, taken in region 2 across the boundary of region 1 and 3, provides the important information of the interface. There are two diffraction patterns in region 2, which correspond to that of the grains in region 1 and 3, indicating that the orientation of the

primary nanocrystals is different. Moreover, two spots with the larger lattice fringe spacing value about 0.4651 nm as marked by the yellow arrows in Fig. 4g, are still not indexed. Did these larger lattice fringes and un-indexed spots belong to a new emerging crystal plane or the overlap of two reflections (Moiré patterns)? It is well known, Moiré patterns can be formed by interfering two sets of lines, and it can be calculated by the following equation [43] (for interpretation of the references to color in this sentence, the reader is referred to the web version of the article):

$$D = \frac{d_1 d_2}{\sqrt{d_1^2 + d_2^2 - 2d_1 d_2 \cos\alpha}} \quad (1)$$

$$\sin\theta = \frac{d_1 \sin\alpha}{\sqrt{d_1^2 + d_2^2 - 2d_1 d_2 \cos\alpha}} \quad (2)$$

where d_1 and d_2 represent the interplanar spacings, the overlapping of them produces the Moiré fringes. α is the angle between two corresponding planes. According to the formula (1) and (2), the larger lattice fringe can be verified. It can be known that the Moiré fringe spacing value (D) and the angle (θ) between Moiré fringes and (3 2 1) planes of LFP are 0.4653 nm and 58.8°, respectively. These results are consisted well with the measured values, which are indicated in Fig. 4e. So it is believed that the larger lattice fringes and two un-indexed spots can be attributed to the Moiré patterns, indicating that no new emerging crystal appear near the GB.

3.2. Formation mechanism

In order to investigate the formation process of spindle-like LFP product (pH 10), time dependent XRD and SEM analysis were carried out. Fig. 5 shows XRD patterns of samples with different reaction times. All peaks for time-dependent samples can be indexed to the orthorhombic phase of LFP, which matches well with the above XRD data (Fig. 1), indicating that the main phase of LFP can be formed at the very beginning (<5 h). However, after a careful comparison, the sample obtained at 5 h contains a trace of impurity phase Li_3PO_4, which results from the process of material synthesis. In the synthesis procedure, two types of liquid precursor (one is $LiOH/H_3PO_4$ suspension; the other is $FeSO_4$/L-ascorbic acid

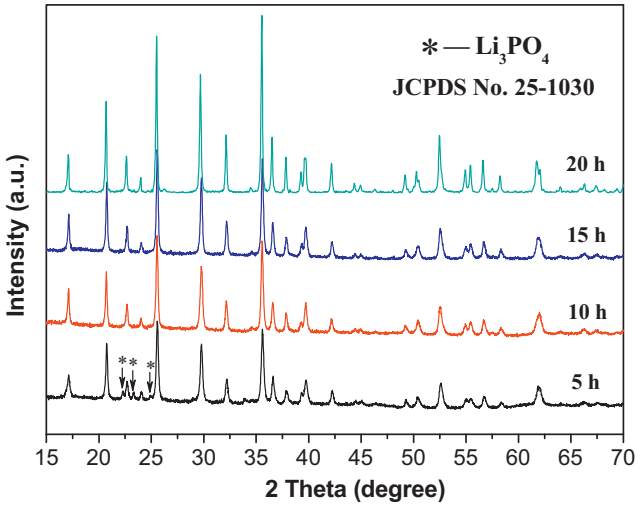

Fig. 5. XRD patterns of the spindle-like samples obtained at different reaction times with pH 10.

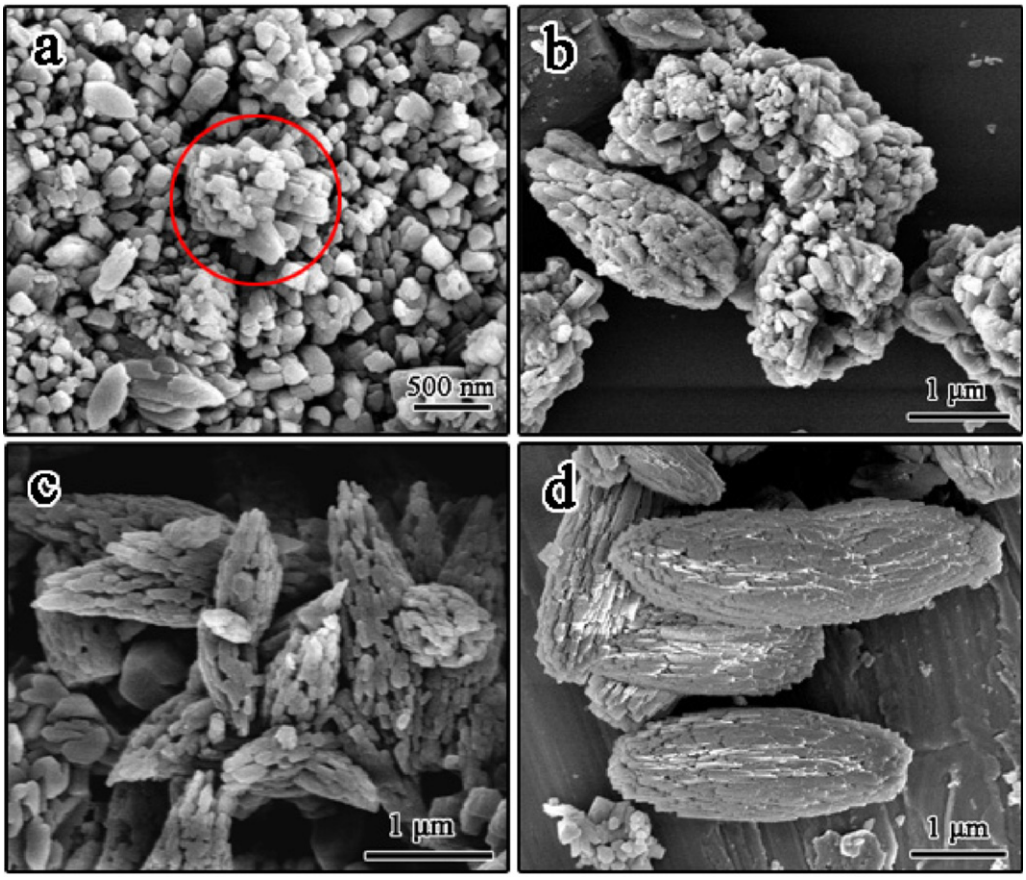

Fig. 6. SEM images of the spindle-like samples obtained with different reaction times: (a) 5 h; (b) 10 h; (c) 15 h; (d) 20 h.

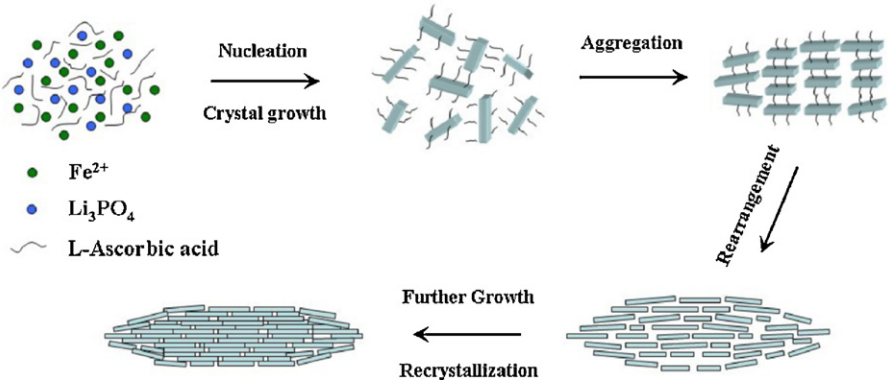

Fig. 7. Schematic illustration of formation mechanism of spindle-like LFP.

mixture) were prepared at first and then mixed together. The relevant chemical reactions in the hydrothermal vessel include two processes:

$$3LiOH + H_3PO_4 = Li_3PO_4 + 3H_2O \quad (3)$$

$$FeSO_4 + Li_3PO_4 = LiFePO_4 + Li_2SO_4 \quad (4)$$

With the gradual vanish of Li_3PO_4 phase, the fully "phase transformation" from Li_3PO_4 to LFP needs a reaction time over 5 h. Furthermore, when the reaction time is increased to 20 h, the intensity of the diffraction peaks of LFP turn to be stronger, suggesting that the crystallinity of the products is improved.

In order to understand the morphological evolution of spindle-like LFP, time dependent SEM analysis was conducted. Fig. 6a–d shows SEM images of the product synthesized after different reaction times. As can be seen from Fig. 6a, most of the products are irregular particles after 5 h reaction. However, a small rectangular structure assembled by irregular nanocrystals can be occasionally observed, which is marked with a red circle in Fig. 6a. After aging for a longer period up to 10 h, the quasi-spindle shaped structures and semi-spindle shaped structures coexist in the as-obtained products (Fig. 6b). When the reaction time extended to 15 h, the spindle-like porous structure could be seen clearly (Fig. 6c). Finally, abundant spindle-like LFP (Fig. 6d) can be obtained when the reaction time is prolonged to 20 h (for interpretation of the references to color in this sentence, the reader is referred to the web version of the article).

Based on the above results, it can be concluded that the intricate crystal growth process of primary nanoparticles proceeds simultaneously with the assembly of as-forming nanocrystals into a 3D hierarchically spindle-like microstructure. The main process is schematically illustrated in Fig. 7. First of all, a great number of Li_3PO_4 precipitations, $FeSO_4$ and L-ascorbic acid mix together. With prolonged reaction time, Li_3PO_4 precipitations begin to change to LFP crystalline nuclei (as shown in Eqs. (3) and (4)). Meanwhile, L-ascorbic acid will be adsorbed at the surfaces of primary LFP crystalline nuclei, which has been reported by Uchiyama and Imai [37]. Driven by the minimization of the total energy of the system, the primary LFP crystalline nuclei tend to aggregate together. Then, Ostwald ripening, as a common phenomenon in crystallization process takes place. According to the Gibbs–Thomson law [44,45], larger LFP crystals grow at the expense of smaller crystalline nuclei. And these LFP nanocrystals intimately contact each other in a side by side manner and tend to rearrange to form a spindle-like microstructure. Finally, LFP nanocrystals will further growth and form a mesoporous spindle-like structure through reducing the total surface energy.

3.3. Electrochemical properties

Fig. 8 shows the cycle performance and charge/discharge profiles of the spindle-like LFP electrode at 0.1 C rate. As shown in Fig. 8a, the spindle-like LFP sample exhibits good cycling stability and high reversible capacity. The charge capacity and discharge capacity are nearly the same, and the charge/discharge efficiency is almost 100%. Fig. 8b displays the charge/discharge curves of the spindle-like LFP electrode at 1st, 10th, 20th, 30th, 40th and 50th cycles. The flat voltage plateaus at 3.4 V and 3.5 V are corresponding to the lithium extraction and insertion respectively, implying the two-phase redox reaction between $FePO_4$ and LFP [19,46]. The sample delivers a high discharge capacity of 163.57 mAh g^{-1} in the first cycle, and could remain 157.32 mAh g^{-1} after 50 cycles.

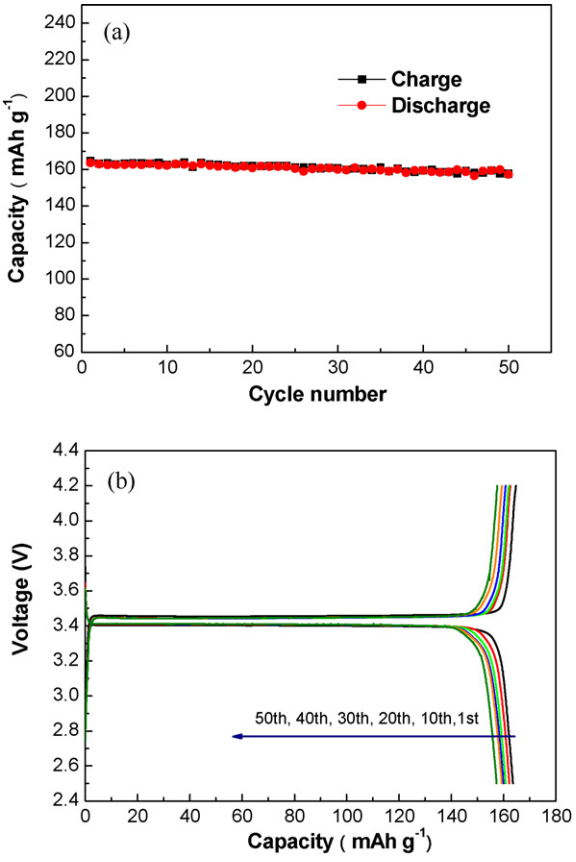

Fig. 8. (a) Cycle performance of the spindle-like LFP electrode at 0.1 C rate. (b) Charge/discharge profiles of the spindle-like LFP electrode at 0.1 C rate.

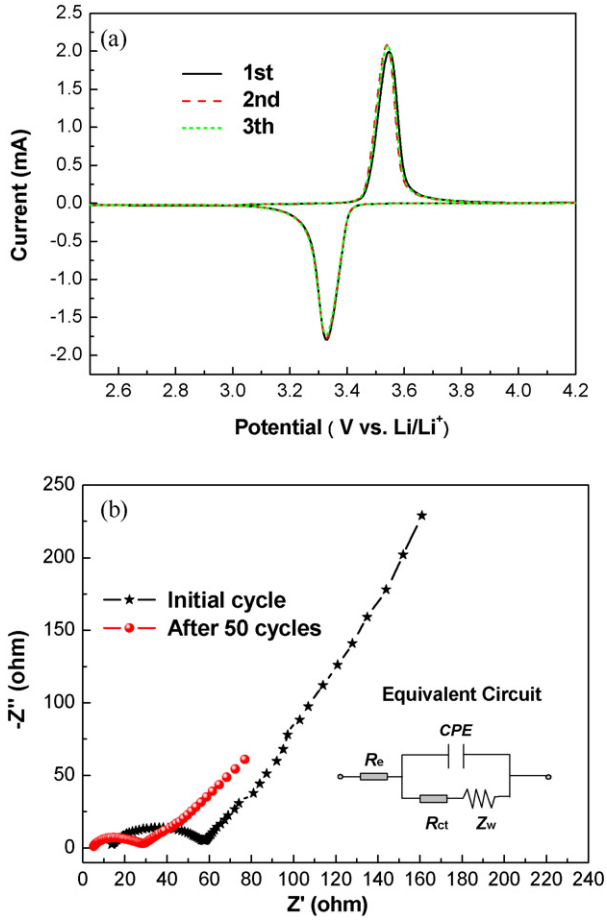

Fig. 9. (a) CV curves of the spindle-like LFP electrodes in the voltage range of 2.5–4.2 V at a scan rate of 0.1 mV s^{-1}. (b) Impedance spectra of the spindle-like LFP electrodes at initial cycle and 50th cycle with the frequency range of 10^{-1} to 10^{6} Hz. The inset is an equivalent circuit of impedance spectra.

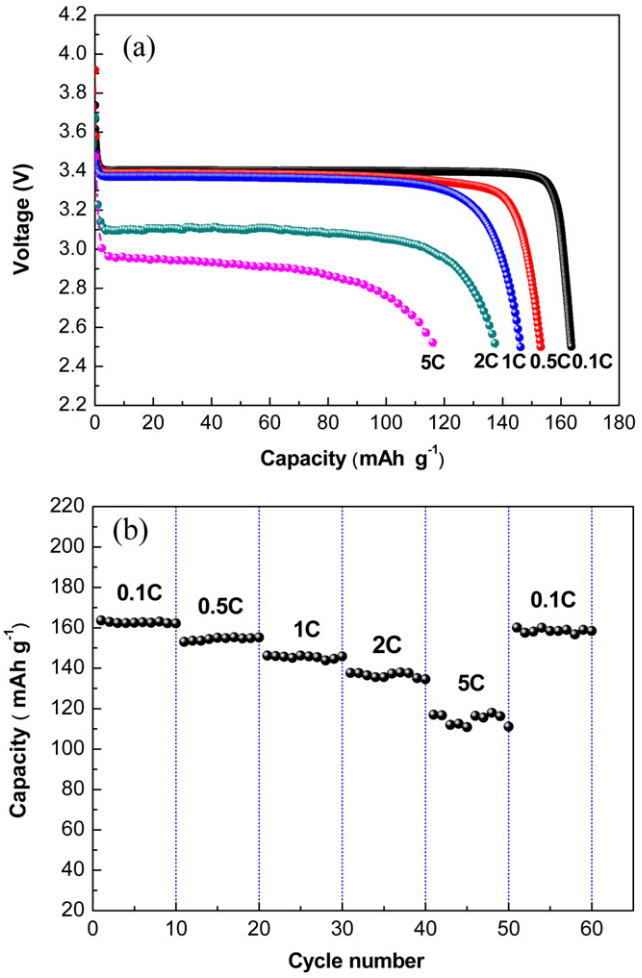

Fig. 10. (a) The charge/discharge profiles of the spindle-like LFP in the voltage from 2.5 to 4.2 V at various current rates. (b) The rate and cycling performances of the spindle-like LFP. The cells were charged at the same rate of 0.1 C to insure identical conditions for each discharge.

In addition, the voltage difference between charge and discharge plateaus has no remarkable increase with the cycle number increasing, suggesting that the spindle-like LFP electrode has good electronic conductivity and high reaction reversibility.

Fig. 9a shows CV curves of the spindle-like LFP electrode. The well-defined and repetitive reduction and oxidation peaks of the spindle-like LFP electrode appear at 3.33 V and 3.54 V, respectively, which are consistent well with the results in Fig. 8b. The small potential separation between the oxidation and reduction peaks of 0.21 V is representative of its good kinetics. The good overlap of the second and third cycles indicates that high electrochemical reversibility has been established after the initial cycle.

Fig. 9b presents the Nyquist plots of the spindle-like LFP electrode. Both profiles exhibit a semicircle and a straight line in the high- and low-frequency regions. As indicated by the inset equivalent circuit in Fig. 9b, the impedance spectra can be explained on the basis of an equivalent circuit with electrolyte resistance (R_e), charge transfer resistance (R_{ct}), double layer capacitance and passivation film capacitance (CPE) and Warburg Impedance (Z_w) [9]. The significant decrease of R_{ct} from 57.7 Ω in the initial cycle to 28.7 Ω after 50 cycles may result from the nanosizing of LFP nanocrystals, which could achieve a higher surface area and reduce the charge transfer resistance.

Fig. 10 shows the remarkable high-rate capability of spindle-like LFP electrode. As shown in Fig. 10a, the discharge capacities of spindle-like LFP at 0.1–5 C rate are 163.57, 153.04, 146.18, 137.66 and 116.98 mAh g^{-1}, respectively. Even at a rate as high as 5 C, the spindle-like LFP sample still has a flat voltage plateau about 3 V, indicating that the spindle-like LFP has a lower polarization and would be well suited for cathode materials of high-power lithium batteries. Fig. 10b exhibits a comparison of the discharge capacity over limited cycling (of 10 cycles each) at different C-rates. The discharge capacity remains stable and decreases regularly with an enhanced discharge rate. The reversible capacities at 0.1, 0.5, 1, 2 and 5 C rate are about 162.17, 155.25, 145.86, 134.59 and 111.04 mAh g^{-1}, which are 99.14, 101.44, 99.78, 97.77 and 94.93% of the initial discharge capacities. In addition, the capacity can be completely recovered when the current density is decreased (0.1 C rate), implying that the spindle-like LFP has good electrochemical reversibility and structural stability.

From the above analysis, these excellent electrochemical performances can be ascribed to the unique microstructure of hierarchical spindle-like LFP. The primary nanocrystals, which constructed the hierarchical architecture, could remain structural stability for the long-term cycling. Furthermore, the porous structure can not only shorten the lithium ion diffusion length, allow better penetration of electrolyte to promote lithium ion diffusion but also increase the electrochemical reaction surface, thus ultimately alleviating electrode polarization. Therefore, this spindle-like LFP can be considered as an excellent cathode material for high-power and high-energy lithium batteries.

4. Conclusion

In this work, self-assembled LFP particles with hierarchical spindle-like microstructure have been successfully synthesized by a facile synthesis route at low temperature. The microstructure and formation process of hierarchical spindle-like LFP particles were investigated by XRD, SEM and TEM. It was found that pH value and reaction time play multifold roles in controlling the morphology of LFP particles. As the cathode material for lithium batteries, the spindle-like LFP sample exhibited excellent electrochemical properties. At 0.1 C rate, the initial discharge capacity was 163.57 mAh g^{-1} (96.22% of the theoretical capacity 170 mAh g^{-1}), and could remain 157.32 mAh g^{-1} after 50 cycles. In addition, the spindle-like LFP sample also displayed good rate performance, even at a rate as high as 5 C, it still had a flat voltage plateau, and delivered a discharge capacity of 116.98 mAh g^{-1}. These improved electrochemical performances can be attributed to the unique mesoporous hierarchical microstructure, which is favorable for increasing the electrochemical reaction surface, enhancing the electronic conductivity, and promoting lithium ion diffusion.

Acknowledgements

This work was supported by the National Natural Science Foundation of China (20673100 and 51002138), the 'Qianjiang Scholars' program of Zhejiang Province, the Natural Science Foundation of Zhejiang Province (Y4090420), the Qianjiang Project of Zhejiang Province (2010R10029), the Merit Based Research Project for Scholars Returning from Abroad and the project sponsored by the Scientific Research Foundation for the Returned Overseas Chinese Scholars (2010609), State Education Ministry.

References

[1] A.K. Padhi, K.S. Nanjundaswamy, J.B. Goodenough, J. Electrochem. Soc. 144 (1997) 1188–1194.
[2] S.Y. Chung, J.T. Bloking, Y.M. Chiang, Nat. Mater. 1 (2002) 123–128.
[3] P.S. Herle, B. Ellis, N. Coombs, L.F. Nazar, Nat. Mater. 3 (2004) 147–152.
[4] A.V. Murugan, T. Muraliganth, A. Manthiram, Electrochem. Commun. 10 (2008) 903–906.
[5] N. Ravet, Y. Chouinard, J.F. Magnan, S. Besner, M. Gauthier, M. Armand, J. Power Sources 97–8 (2001) 503–507.
[6] S.F. Yang, Y.N. Song, P.Y. Zavalij, M.S. Whittingham, Electrochem. Commun. 4 (2002) 239–244.
[7] Y.H. Huang, J.B. Goodenough, Chem. Mater. 20 (2008) 7237–7241.
[8] S.W. Oh, S.T. Myung, S.M. Oh, K.H. Oh, K. Amine, B. Scrosati, Y.K. Sun, Adv. Mater. 22 (2010) 4842–4845.
[9] W.K. Zhang, X.Z. Zhou, X.Y. Tao, H. Huang, Y.P. Gan, C.T. Wang, Electrochim. Acta 55 (2010) 2592–2596.
[10] Z.J. Wu, H.F. Yue, L.S. Li, B.F. Jiang, X.R. Wu, P. Wang, J. Power Sources 195 (2010) 2888–2893.
[11] M. Wagemaker, B.L. Ellis, D. Luetzenkirchen-Hecht, F.M. Mulder, L.F. Nazar, Chem. Mater. 20 (2008) 6313–6315.
[12] X.Q. Ou, G.C. Liang, L. Wang, S.Z. Xu, X. Zhao, J. Power Sources 184 (2008) 543–547.
[13] H. Liu, Q. Cao, L.J. Fu, C. Li, Y.P. Wu, H.Q. Wu, Electrochem. Commun. 8 (2006) 1553–1557.
[14] K. Zaghib, P. Charest, M. Dontigny, A. Guerfi, M. Lagace, A. Mauger, M. Kopec, C.M. Julien, J. Power Sources 195 (2010) 8280–8288.
[15] Y.G. Xia, M. Yoshio, H. Noguchi, Electrochim. Acta 52 (2006) 240–245.
[16] E.M. Bauer, C. Bellitto, G. Righini, M. Pasquali, A. Dell'Era, P.P. Prosini, J. Power Sources 146 (2005) 544–549.
[17] C. Delacourt, P. Poizot, S. Levasseur, C. Masquelier, Electrochem. Solid State Lett. 9 (2006) A352–A355.
[18] D.H. Kim, J. Kim, Electrochem. Solid State Lett. 9 (2006) A439–A442.
[19] M. Konarova, I. Taniguchi, J. Power Sources 195 (2010) 3661–3667.
[20] Y.G. Wang, Y.R. Wang, E.J. Hosono, K.X. Wang, H.S. Zhou, Angew. Chem., Int. Ed. 47 (2008) 7461–7465.
[21] D. Choi, P.N. Kumta, J. Power Sources 163 (2007) 1064–1069.
[22] C.R. Sides, F. Croce, V.Y. Young, C.R. Martin, B. Scrosati, Electrochem. Solid State Lett. 8 (2005) A484–A487.
[23] G. Arnold, J. Garche, R. Hemmer, S. Strobele, C. Vogler, A. Wohlfahrt-Mehrens, J. Power Sources 119 (2003) 247–251.
[24] S. Franger, F. Le Cras, C. Bourbon, H. Rouault, J. Power Sources 119 (2003) 252–257.
[25] J.K. Kim, G. Cheruvally, J.W. Choi, J.U. Kim, J.H. Ahn, G.B. Cho, K.W. Kim, H.J. Ahn, J. Power Sources 166 (2007) 211–218.
[26] H.C. Shin, W.I. Cho, H. Jang, J. Power Sources 159 (2006) 1383–1388.
[27] M. Konarova, I. Taniguchi, J. Power Sources 194 (2009) 1029–1035.
[28] K. Dokko, S. Koizumi, H. Nakano, K. Kanamura, J. Mater. Chem. 17 (2007) 4803–4810.
[29] A. Kuwahara, S. Suzuki, M. Miyayama, J. Electroceram. 24 (2010) 69–75.
[30] T. Muraliganth, A.V. Murugan, A. Manthiram, J. Mater. Chem. 18 (2008) 5661–5668.
[31] A.V. Murugan, T. Muraliganth, A. Manthiram, J. Phys. Chem. C 112 (2008) 14665–14671.
[32] J.F. Ni, M. Morishita, Y. Kawabe, M. Watada, N. Takeichi, T. Sakai, J. Power Sources 195 (2010) 2877–2882.
[33] G. Yang, H.M. Ji, H.D. Liu, K.F. Huo, J.J. Fu, P.K. Chu, J. Nanosci. Nanotechnol. 10 (2010) 980–986.
[34] K. Saravanan, M.V. Reddy, P. Balaya, H. Gong, B.V.R. Chowdari, J.J. Vittal, J. Mater. Chem. 19 (2009) 605–610.
[35] H. Yang, X.L. Wu, M.H. Cao, Y.G. Guo, J. Phys. Chem. C 113 (2009) 3345–3351.
[36] J.F. Qian, M. Zhou, Y.L. Cao, X.P. Ai, H.X. Yang, J. Phys. Chem. C 114 (2010) 3477–3482.
[37] H. Uchiyama, H. Imai, Cryst. Growth Des. 10 (2010) 1777–1781.
[38] D. Rangappa, K. Sone, T. Kudo, I. Honma, J. Power Sources 195 (2010) 6167–6171.
[39] F. Teng, S. Santhanagopalan, A. Asthana, X.B. Geng, S.I. Mho, R. Shahbazian-Yassar, D.D. Meng, J. Cryst. Growth 312 (2010) 3493–3502.
[40] Y.D. Cho, G.T.K. Fey, H.M. Kao, J. Power Sources 189 (2009) 256–262.
[41] Z.L. Wang, S.R. Su, C.Y. Yu, Y. Chen, D.G. Xia, J. Power Sources 184 (2008) 633–636.
[42] F. Yu, J.J. Zhang, Y.F. Yang, G.Z. Song, J. Power Sources 195 (2010) 6873–6878.
[43] M. Han, M. Tanaka, M. Takeguchi, Q. Zhang, K. Furuya, J. Cryst. Growth 255 (2003) 93–101.
[44] Y.Y. Li, J.P. Liu, X.T. Huang, G.Y. Li, Cryst. Growth Des. 7 (2007) 1350–1355.
[45] J.G. Yu, H.T. Guo, S.A. Davis, S. Mann, Adv. Funct. Mater. 16 (2006) 2035–2041.
[46] B.F. Wang, Y.L. Qiu, S.Y. Ni, Solid State Ionics 178 (2007) 843–847.